

Realization of Large Area $\text{Co}_{20}\text{Fe}_{60}\text{B}_{20}$ -Based Perpendicular Magnetic Tunnel Junction for CMOS Compatible Device Application

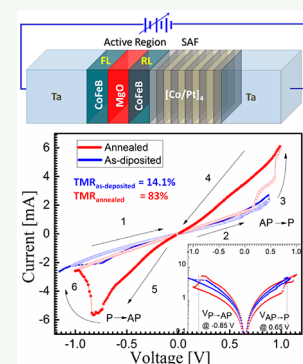
Mohamad G. Moinuddin, Aijaz H. Lone, Srikant Srinivasan, and Satinder K. Sharma*

School of Computing and Electrical Engineering, Indian Institute of Technology (IIT) Mandi, Mandi-175005 (Himachal Pradesh), India

Supporting Information

ABSTRACT: This study reports the current-induced switching of a $\text{Co}_{20}\text{Fe}_{60}\text{B}_{20}/\text{MgO}/\text{Co}_{20}\text{Fe}_{60}\text{B}_{20}$ -based perpendicular magnetic tunnel junction (p-MTJ) with a $[\text{Co}/\text{Pt}]_4$ stack as a synthetic anti-ferromagnetic (SAF) layer. Electrical and spectroscopic evidence of p-MTJs reveals that the pinning of the $\text{Co}_{20}\text{Fe}_{60}\text{B}_{20}$ layer by the SAF through a Ta spacer layer enhances the switching resistance after annealing at 650 K (375 °C). A drastic improvement of 6 times in the tunneling magnetoresistance (TMR) was observed after annealing in an external magnetic field (14% for as-deposited and 83% for annealed both for zero bias). The TMR also shows a gradual increased behavior with bias at room temperature, which may be attributed to the multi-domain switching with increase in current. The analogous SAF-based MTJ devices were modeled using the non-equilibrium Green's function (NEGF) to validate the experimental results. The existence of a stable TMR and the low switching current density of the fabricated p-MTJ structures provides higher reliability and low-power operation. This makes it attractive for next-generation MTJ applications, especially for embedded memory, system-on-chip, IoT, and neuromorphic computing applications.

KEYWORDS: perpendicular magnetic tunnel junction, increasing tunneling magnetoresistance, synthetic anti-ferromagnetic, low switching current density, non-equilibrium Green's function



1. INTRODUCTION

Emerging magnetoresistive random access memory (MRAM),¹ involving the integration of magnetic tunnel junction (MTJ) and CMOS technology, is a promising alternative for the existing nonvolatile semiconductor memory (NVM) applications, such as NAND Flash and others.^{2–4} In particular, MRAM shows much promise due to low power consumption, high endurance, and fast switching performance.⁵ The current challenges of MRAM lie in uniform resistance controllability, reliable switching of magnetic bits, and integration of MTJ with CMOS technology.^{6,7}

There is considerable interest to explore new CMOS compatible MRAM systems with novel functionalities like spin-transfer torque (STT), spin-orbit torque (SOT), and domain wall motion (DWM) for improved magnetic switching.⁸ Among all NVMs, STT-RAM has demonstrated the highest endurance ($>10^{12}$ cycles) and thermal compatibility for embedded back-end of line (BEOL) processed device applications, such as cache, big data memory, and high-end SoC.^{9,10} The foremost hindrances for realizing the real-world application of STT-RAM devices are the development of compatible magnetic materials, high-temperature stability, reliable switching, and device fabrication technology in line with an existing CMOS.^{11,12} For scalable and reliable STT-RAM, a low error probability obtained from the ratio of on and off currents is an important metric.¹³ In an MTJ, this ratio is reflected in the tunneling magnetoresistance (TMR) and usually decreases with bias. For stand-alone memory, TMR

needs to be greater than 200%. While subjected to high-temperature reaching 673 K (400 °C) or beyond for extended hours in the BEOL process, slightly lower TMR values of fabricated p-MTJs are considered to still be reliable for embedded memory application.¹⁴

In pursuit of attaining a high TMR, hitherto numerous ferromagnetic (FM)/oxide interfaces have been analyzed for symmetry filtering of tunneling current such as $\text{Fe}/\text{Al}_2\text{O}_3$, Co/AlO_x , Fe/CrO_2 , Fe/MgO , Co/MgO , and CoFeB/MgO .¹⁵ Among these, the half Heusler alloy ABX geometry, e.g., CoFeB has demonstrated high spin polarization ($\sim 65\%$) with perpendicular magnetic anisotropy (PMA).¹⁶

However, the stray field induced in the CoFeB/MgO -based MTJ system results in the asymmetric switching of the free layer by reducing the stability of the antiparallel state.¹⁴ This concern was addressed to a large extent by coupling of the reference FM layer with a synthetic anti-ferromagnetic (SAF) layer (consisting of FM/heavy metal (HM)/FM).¹⁷ This FM/HM/FM stacking serves as a synthetic magnetic ordering isomorphous to a layered anti-ferromagnetic film. Carvello et al. reported the fcc (111) L_{10} FePt , $[\text{Co}/\text{Pd}]_n$, and $[\text{Co}/\text{Pt}]_n$ structures for SAF, which all result in perpendicular magnetic anisotropy.¹⁸ The presence of effective 3d–5p coupling between FM and HM layers in the FM/HM/FM structure

Received: July 26, 2019

Accepted: October 25, 2019

Published: October 25, 2019

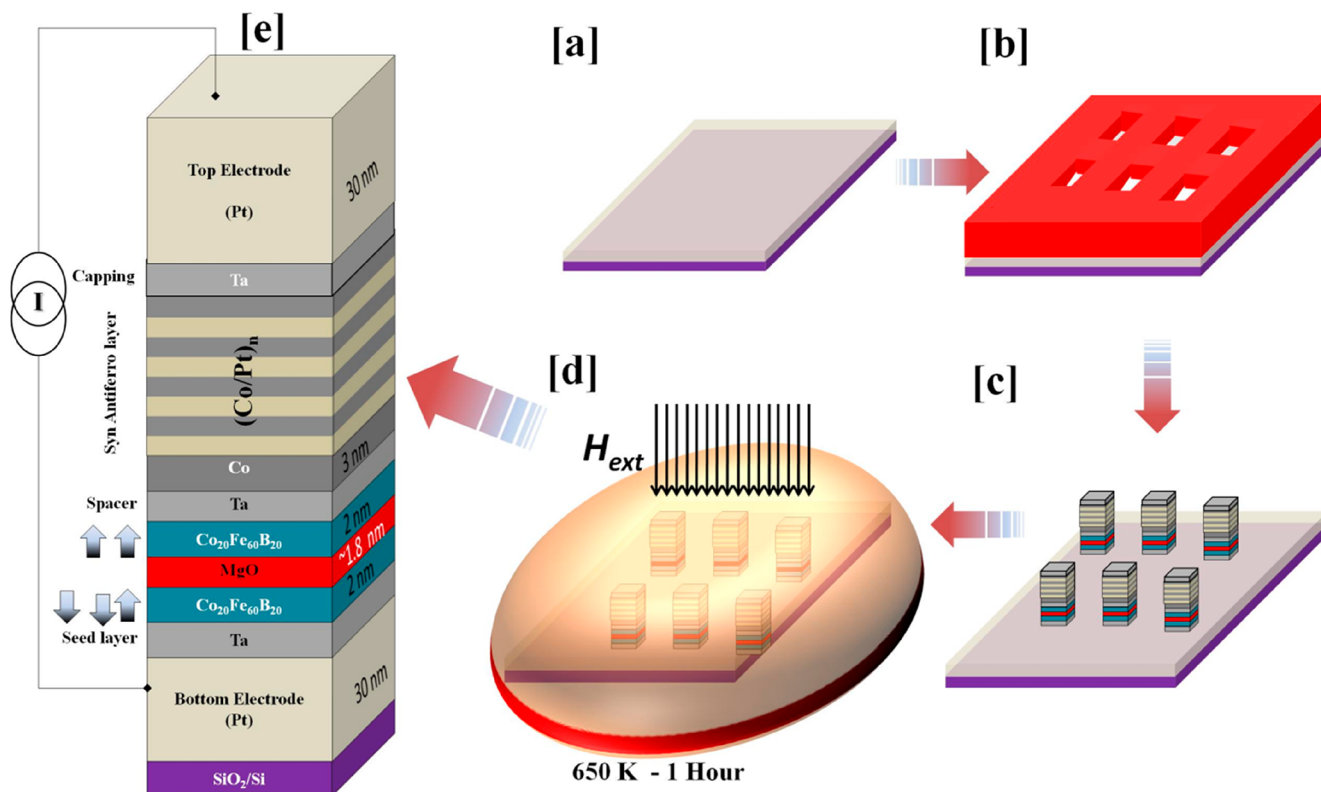


Figure 1. Schematic process flow of p-MTJ fabrication and investigation of fabricated device structures; (a) deposition of bottom electrode pad of Pt/Ti. (b) Trench formation through 365 nm photolithography. (c) Deposition of MTJ stacks. (d) Annealing of MTJ in external perpendicular magnetic field at 650 K. (e) Schematic of complete STT-based p-MTJ with layers labeled as seed layer Ta, $Co_{20}Fe_{60}B_{20}$ free layer, MgO tunneling layer, $Co_{20}Fe_{60}B_{20}$ reference layer, Ta spacer, $Co/[Pt/Co/Pt]_4$ SAF pinning layer, and Ta capping layer.

favors either parallel or antiparallel magnetization configuration of two corresponding FM layers depending upon the spacer thickness.^{19–21} Also, stacked SAF layers with the FM layer below a certain of a thickness (e.g., $Co < 2$ nm) have shown PMA with considerable anti-ferromagnetic behavior and thermal stability.²² The aforementioned developments have led to both high thermal stability and high TMR. In turn, this has paved the way for higher temperature device processing and reduced device dimensions allowing a CMOS–p-MTJ compatible memory cell (1T-1R) for a next-generation technology node.²³

The present work demonstrates field-free STT controlled switching of Ta/ $[Co/Pt]_4/Co/Ta/Co_{20}Fe_{60}B_{20}/MgO/Co_{20}Fe_{60}B_{20}/Ta$ -based p-MTJ system with enhanced TMR at room temperature for nonvolatile memory application. The behavior of a single SAF $[Co/Pt]_n$ has been extensively studied and used for pinning and thermal stabilization of the $Co_{20}Fe_{60}B_{20}$ reference layer (RL) while reducing the device structure complexity and effective height.²⁴ Further, the experimental results are supported by the nonequilibrium Green's function (NEGF) and the theory of interlayer exchange coupling-based simulations.

2. MATERIALS AND METHODS

2.1. Materials and Fabrication. In order to investigate the current-induced switching (CIS) in CoFeB-based p-MTJ structures, a set of devices were fabricated as per the process flow as shown in Figure 1a–d. The standard MTJ blanket was as follows: Pt(30)/Ta(5)/ $[Co/Pt]_4/Co/Ta/Co_{20}Fe_{60}B_{20}(2)/MgO(1.8)/Co_{20}Fe_{60}B_{20}(2)/Ta(05)/Pt(30)/Ti(10)/SiO_2(300)/Si$ (the number mentioned in parentheses indicate the thickness of layers in nm). The p-MTJ layers

were deposited over a thermally oxidized silicon substrate using multitarget DC and RF plasma sputtering system at a base pressure of 5.0×10^{-7} mbar. As depicted in Figure 1e, the multilayer device structure consists of Ta (05) seed layer; $Co_{20}Fe_{60}B_{20}$ (2) free layer (FL); MgO (1.8) tunneling layer; $Co_{20}Fe_{60}B_{20}$ (2) reference layer; Ta (1.2) spacer; $Co/[Pt/Co/Pt/Co/Pt/Co/Pt/Co]$ SAF pinning layer (presented as $Co/[Pt/Co/Pt]_4$ in this Article); and Ta (5) capping layer. Figure 1a–d shows the subsequent device processing steps: multistep standard photolithography, thin-film stack deposition, annealing and metallization of various processing steps. In this process, the bottom Pt/Ti (30/5) electrode was deposited over a standard RCA cleaned, thermally oxidized Si wafer, which was followed by typical standard photolithographic steps to pattern $50 \times 50 \mu m^2$ trenches over a positive photoresist. The whole MTJ blanket was deposited over the patterned substrate at 300 K and at a base pressure of $\sim 9.0 \times 10^{-7}$ mbar. $Co_{20}Fe_{60}B_{20}$ FM layers were deposited from a CoFeB (1:3:1) alloy target using 90 W, argon (Ar) plasma-based RF magnetron sputtering at 5×10^{-3} mbar. A MgO tunnel barrier was also sputtered from a 99.99% pure single crystal MgO target and sandwiched between the free and reference layer. Thereafter, the layers of $[Co/Pt]_4$ were deposited as Co (RF) and Pt (DC) co-sputtering from 99.999% pure Co and Pt targets over the rotating substrate. Afterward, a lift-off process was performed for realization of final p-MTJ structures from the deposited blanket. These p-MTJ stacks were annealed at 650 K (375 °C) under a 1 kOe perpendicular magnetic field at a vacuum of 10^{-6} mbar to achieve the PMA as shown in Figure 1d.

The study of the surface morphology and spectroscopic investigations are accomplished using field emission scanning electron microscopy (FE-SEM, Nova FEI), X-ray diffraction (XRD) spectroscopy (Bruker), X-ray photoelectron spectroscopy (XPS, Thermo-Scientific), vibrational sample magnetometry (VSM, Quantum Design), and atomic force microscopy (AFM, Bruker), whereas the

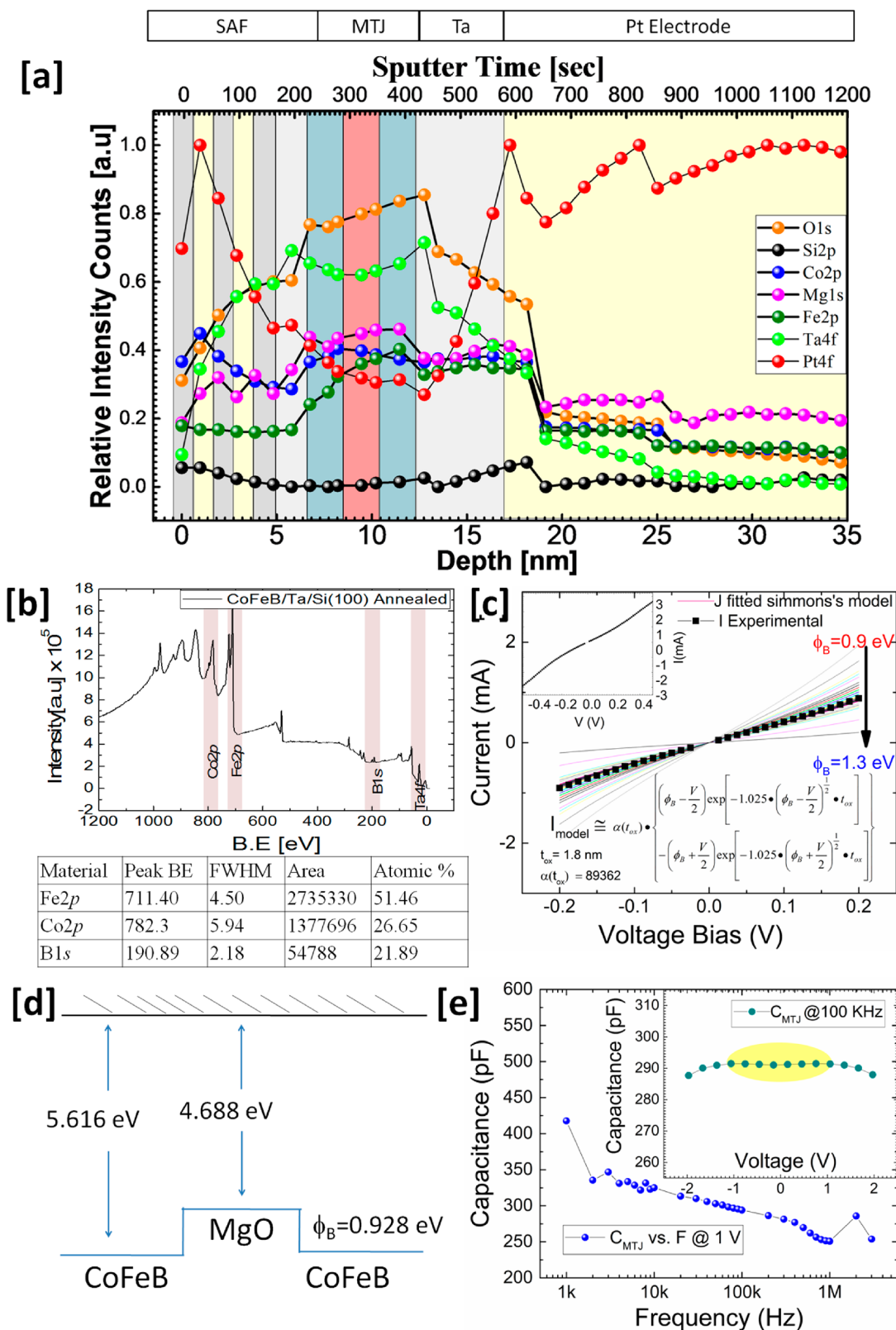


Figure 2. Fabricated p-MTJ devices. (a) XPS depth profile of annealed p-MTJ device stack with Pt bottom layer; all core spectra analyzed with 500 eV etch energy Ar⁺ plasma. (b) Free layer CoFeB material distribution. (c) Tunnel current investigation across the barrier; the *I*–*V* characteristics were fitted with a modified Simmons’ expression for low bias; the spectra show a good fit for 1.06 eV (thick black); the inset shows the experimental tunnel current. (d) Barrier height calculated with ultraviolet photoelectron spectra for individual materials show the ϕ_B of 0.93 eV. (e) Capacitive behavior analyzed across the tunnel barrier; the main panel shows the frequency–capacitance response for a 25 mV AC signal, and inset shows a stable capacitance at 100 kHz.

fabricated p-MTJ structures were analyzed using the four-probe $I-V$ measurement tool, Keithley 4200 SCS.

2.2. Modeling and Theoretical Analysis. To study the transport characteristics of the device, an effective mass tight-binding (EMTB) model was used to represent the Hamiltonian of the active region (CoFeB/MgO/CoFeB), and non-equilibrium Green's function (NEGF)-based spin transport simulations were conducted for the fabricated p-MTJ structures, following existing MTJ theory.²⁵ The different device characteristics studied include the current versus voltage ($I-V$) characteristics, resistance versus voltage ($R-V$) characteristics, and an estimation of different spin torques acting on the FL. Following the mode space analysis, a device model Hamiltonian consisting of a one-dimensional (1D) discrete chain of lattice points with lattice spacing $a_{fm} = 2.858 \text{ \AA}$ (CoFeB lattice constant) and $a_{mgo} = 4.2 \text{ \AA}$ was set up for each transverse mode described by wave vector k_r . These lattice parameters were extracted from crystallographic analyses of CoFeB and MgO. Other material parameters used in simulation are^{8,26} the Fermi level of CoFeB (2.25 eV), the exchange splitting in CoFeB (2.15 eV), the barrier height (ϕ_B) between CoFeB and MgO (0.9–1.2 eV), the effective mass of the electron in CoFeB ($0.8m_0$), and the effective mass of electron in MgO ($0.33m_0$); here, m_0 corresponds to the free electron mass. These values are used with a small modification justified by some band structure nonidealities.²⁵ This single band Hamiltonian matrix effectively describes the device behavior in terms of hopping parameters t_{fm} and t_{mgo} , where $t = (\hbar^2/2ma^2)$ and \hbar = the reduced Planck's constant, m = effective mass, and a = lattice constant. The coupling of a semi-infinite electrode with the device is modeled in terms of self-energy,⁴ for the left and right contact self-energy matrices Σ_L and Σ_R were calculated and along with H used in the expression for the retarded Green's function (eq 1)

$$G = [(E + i0^+)I - H - \Sigma_L - \Sigma_R]^{-1} \quad (1)$$

The broadening matrices of the left and right (eqs 2a and 2b) contacts are expressed as

$$\Gamma_L = i(\Sigma_L - \Sigma_L^+) \quad (2a)$$

$$\Gamma_R = i(\Sigma_R - \Sigma_R^+) \quad (2b)$$

The density spectral function A , from which we compute local density of states of the device, is given by

$$A_L(E) = G\Gamma_L G^+ \text{ and } A_R(E) = G\Gamma_R G^+ \quad (3)$$

Similarly, local electron density is obtained from the diagonal element of the electron correlation function matrix given by

$$G^n = A_L f_L + A_R f_R \quad (4)$$

which is used in the transport equation (eq 5) along with other computed matrices to numerically compute the charge current and spin current versus voltage characteristics of the MTJ. The different current components are calculated with the expression.

$$I_{(y)} = \text{trace}(Y I_{op}) \quad (5)$$

Here, Y represents the identity matrix for charge current, and the Pauli spin matrix σ represents spin current.^{5,4} The current density operator is expressed as

$$I_{op} = \frac{i}{\hbar} \left\{ (HG^n - G^n H^+) + \left(\sum G^n - G^n \sum^+ \right) + \left(\sum^{in} G^+ - G \sum^{in} \right) \right\} \quad (6a)$$

$$I = \frac{i}{\hbar} \sum_{k_t} \left\{ (HG^n - G^n H^+) + (\Sigma G^n - G^n \Sigma^+) + \left(\sum^{in} G^+ - G \sum^{in} \right) \right\} \quad (6b)$$

Finally considering coherent transport and conservation of the transverse momentum vector (k_{\parallel}), the 3D structure, which has been effectively modeled as 1D paralleled and uncoupled transverse modes, allows us to compute current for each transverse mode individually from eq 6b over the energy range ($E_f \pm 10k_B T$), where k_B is the Boltzmann constant, and T is the temperature (assumed 300 K). Finally, the currents at different transverse energies were integrated with respect to transverse energy. It is to be noted that small adjustments were done in m_{ox} and $U_b(\phi_B)$ within the range prescribed in ref 25 to get a close agreement with experimental data.

3. RESULTS AND DISCUSSION

The morphology analyses of fabricated p-MTJ devices were performed to confirm the uniform surface topography and also to compute the device dimensions. FE-SEM micrographs (top-down) for p-MTJ device structures of $\sim 50 \times 50 \mu\text{m}^2$ along with a device stack thickness (avg $t_{mtj} \approx 22 \text{ nm}$) profile are shown in Figure S1a,b. The $\text{Co}_{20}\text{Fe}_{60}\text{B}_{20}$ free FL's surface roughness as measured by AFM is shown in Figure S1c and found to be $\sim 0.5 \text{ nm}$ (r.m.s), which confirms the smooth oxide/FL interface. To reveal the high-quality interface and existence of $[\text{Co}/\text{Pt}]_4\text{SAF}$ after annealing of the thin-film stack, XPS depth profiling analyses for $[\text{Co}/\text{Pt}]_4/\text{Co}/\text{Ta}/\text{C}_{20}\text{Fe}_{60}\text{B}_{20}(2)/\text{MgO}(1.8)/\text{C}_{20}\text{Fe}_{60}\text{B}_{20}(2)/\text{Ta}(05)/\text{Pt}(30)$ were performed. Figure 2a shows the traces for each material of the MTJ blanket with relative concentration at the given depth.²⁷ The interface position indicated in Figure 2a clearly depicts the layer distribution in the MTJ structure.^{22–24,28} To establish perpendicular magnetic anisotropy (PMA), the material composition distribution in iron-enriched CoFeB was analyzed by XPS over a control sample (CoFeB/Ta/Si). The atomic distribution of Fe:Co:B was found 51.46:26.5:21.89 %, as shown in Figure 2b. The tunneling charge transport analysis from experimental data clearly suggests a nonlinear transmission across the p-MTJ barrier MgO (1.8 nm). Figure 2c (inset) depicts the experimental data (thick black line) for tunneling across MgO. Here, the barrier height of MgO was determined using a modified Simmons' expression for low bias as shown in Figure 2c.^{29,30} The fitted model indicates a tunnel barrier $\phi_B \approx 1.068 \text{ eV}$ (details of the fitting parameter explained in Figure S3), which was further analyzed through valence band spectral analysis. The work function (ϕ) of the $\text{Co}_{20}\text{Fe}_{60}\text{B}_{20}/\text{MgO}/\text{Co}_{20}\text{Fe}_{60}\text{B}_{20}$ structure was extracted from the ultraviolet photoelectron spectroscopy (UPS) measurements using the He^+ source of 21.2 eV for MgO and CoFeB, and they were found to be 4.688 and 5.616 eV, respectively. The barrier height computed for $\text{Co}_{20}\text{Fe}_{60}\text{B}_{20}/\text{MgO}$ is 0.928 eV as inferred from Figure 2d, which is in close agreement with the ϕ_B obtained from fitting the electrical characteristics.³¹

The major issue of a large area MTJ is film uniformity and pinhole formation due to metal diffusion or tunnel barrier discontinuity, which leads to the anomalous variation in the TMR as reported by Useinov et al.³² The electrical reliability of MgO as a tunnel barrier has been established by considering the fabricated MTJ stack as analogous to an MIM system. Charge accumulation at the FM/MgO interface provides significant capacitance. Figure 2e shows the capacitance of tunnel barrier across a substantial range of AC signal frequency ($25 \text{ mV} \times \cos(\omega t)$) superimposed over the DC signal. It was found that this capacitance reduces with strong dependence at low frequency ($f_{low} < 10 \text{ kHz}$) and weak dependence at high frequency ($f_{high} > 50 \text{ kHz}$). At high frequency (100 kHz), the p-MTJ has shown a stable capacitance of $291 \pm 1 \text{ pF}$ ($11.64 \pm$

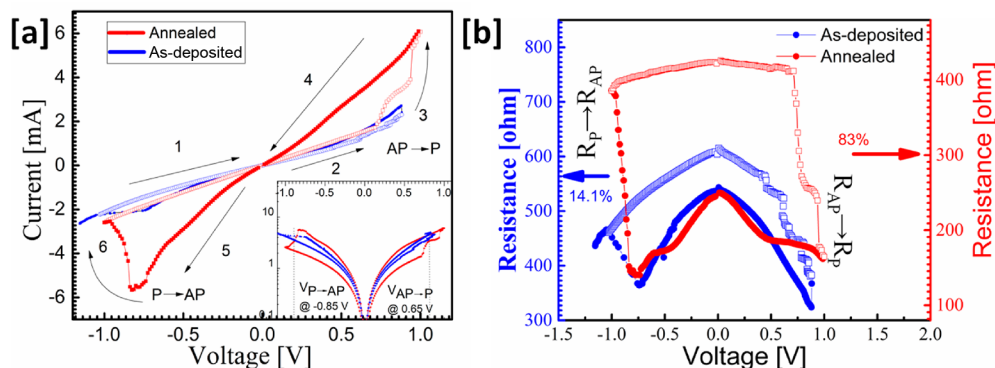


Figure 3. Current controlled switching characteristics for fabricated p-MTJ structures. (a) I – V characteristic of p-MTJ with different resistive paths (AP: antiparallel and P: parallel); bias switching shown as $V_{P \rightarrow AP} = -0.85$ V and $V_{AP \rightarrow P} = 0.65$ V, respectively, in $\log(I)$ vs V characteristics (inset). (b) Resistance vs voltage plot for P and AP configurations; an enhanced TMR of 83% was observed at zero bias.

$0.1 \mu\text{F}/\text{cm}^2$) within a device operation bias of $-1 \rightarrow +1$ V, which depicts the linear q – V relation without bias dependent charge dissipation inside the tunnel barrier. Moreover, there are a few reports regarding the magnetocapacitance at low-frequency AC signal analysis for MgO-based MTJs, which has to be systematically analyzed in a future publication.^{33,34}

3.1. Current-Induced Switching Analysis. Figure 3a shows the measured I – V characteristics of Ta/[Co/Pt]₄/Co/Ta/Co₂₀Fe₆₀B₂₀/MgO/Co₂₀Fe₆₀B₂₀/Ta structures in the absence of an external magnetic field, demonstrating current-induced switching (CIS) of the FL due to spin torque exerted by the RL.³² As depicted in Figure 3a, the Co₂₀Fe₆₀B₂₀-based p-MTJ device follows the antiparallel (AP) and parallel (P) current paths when sweeping from -1 to 1 V ($1 \rightarrow 2 \rightarrow 3$) and from 1 to -1 V ($4 \rightarrow 5 \rightarrow 6$), respectively. It reveals the different resistance states of the p-MTJ device at the forward and reversed current directions. These resistance paths correspond to the parallel (P) and antiparallel (AP) magnetization states of the FL with respect to the RL.³³ The applied biases to change the resistance states of p-MTJ structures from the parallel to the antiparallel state and vice versa were found to be $V_{P \rightarrow AP} = -0.85$ V and $V_{AP \rightarrow P} = 0.65$ V, respectively (as shown in Figure 3a (inset)). This asymmetric response of switching voltage is explained by the voltage asymmetry of the spin–transfer torque on the FL.^{25,35,36} It was also observed that after annealing, the tunneling current is enhanced in the device. The amorphous tunnel barrier has higher electron scattering inside the barrier, resulting in high barrier resistance and low TMR.^{37,38}

The calculated $\text{TMR} = \frac{R_{AP} - R_P}{R_P}$ from Figure 3b for as-deposited p-MTJ was found to be 14.1%, whereas for the annealed p-MTJ, the TMR increased to 83%. The annealing enhances the crystallinity of the ferromagnets and MgO and the quality of the interface between FM and MgO. The improved quality of the oxide and interface improves the band filtering property of MgO and the interface, thus enhancing the TMR up to 83%. Moreover, the improved crystallinity of the FM reduces the number of domains, leading to increased stability. This, in turn, increases the switching current for the annealed device to 6 mA, as compared to 2 mA in the as-deposited case. To understand the tunneling mechanism in the amorphous and annealed system, we have analyzed the blanket p-MTJ with different spectroscopic investigations (discussed later in Section 3.2).^{39,40}

As shown in Figure 3b, a TMR of 83% was achieved at zero bias and was found to increase slightly with increasing bias. The resistance states of p-MTJ structures were found to be stable within the read voltage bias of ± 0.2 V.¹⁵ Thus, the existence of a stable TMR and low switching current density in the fabricated p-MTJ structures provides higher reliability with regard to long cycle data retention and low-power operation. This makes it attractive for next-generation MTJ applications, especially for embedded memory and system-on-chip applications, where it has to sustain high-temperature CMOS (BEOL) processing.

Based on the analysis described above, a switching schematic is proposed that consists of four different configurations of the multidomain FL under distinct bias conditions as shown in Figure S5.⁴¹ Due to the multi-domain existence in FL, at zero bias, some domains are not properly aligned toward both P and AP states, which results in the reduced effective magnetization of FL. The zero-bias resistance corresponds to this average effective magnetization orientation between FL and RL. While increasing bias in the AP state from $0 \rightarrow 0.65$ V, we observe almost a bias independent resistance state and the multi-level switching until complete magnetization reversal to the P state as shown in Figure 3b. In the reverse direction starting from the P state, $0.65 \rightarrow -0.8$ V, we observe a nonlinear path due to the alignment of residual domains, and finally, switching from P to AP is abrupt and occurs at a large bias of -0.8 V. The different resistance trends with varying bias for the P and AP paths may be attributed to the dominance of the ferromagnetic type interlayer exchange coupling between RL and FL, which makes the parallel state stable. Also, the voltage asymmetry of STT due to bias dependence of spin polarization results in this asymmetrical switching.⁴¹

Since the real chips may operate at elevated temperatures, a high-temperature aging is usually performed to match standard CMOS process conditions. The fabricated MTJ has been analyzed for the temperature range from 296 to 380 K. A temperature ramp rate of 0.25 K/s was applied along with the retention cycle to witness the p-MTJ thermal stability. Figure 4 shows real-time resistance (R_P) analysis for a read bias of 0.2 V.

Initially, the MTJ was found in the parallel state with the R_P of $\sim 160 \Omega$ and found stable up to ~ 353 K ($\sim 80^\circ\text{C}$). The effect of temperature variation on the magnetization stability of FL and RL is already well-known. Further, the increasing temperatures also alter the coupling between SAF and RL, which in turn results in the FL switching (as perceived from Figure S6).⁴² Nevertheless, the stable resistance state up to

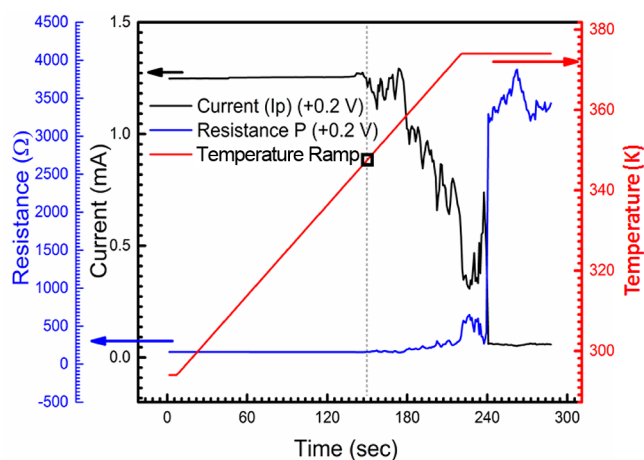


Figure 4. Resistance state stability of fabricated p-MTJ under increasing temperature.

~353 K for the fabricated p-MTJ was found suitable for CMOS embedded applications.

The device was modeled using known theory to realize the TMR behavior of the fabricated MTJ. Figure 5a shows the active region for the modeled MTJ. Figure 5b shows the parabolic approximation of energy bands including the various transverse modes, based on the effective mass tight-binding model for the active region of the MTJ (CoFeB/MgO/CoFeB). The I - V and R - V characteristics were computed by

the effective mass band tight-binding (EMTB) non-equilibrium Green's function-based spin transport model. The assumption of a coherent interface between MgO and CoFeB allows us to use the mode space approach to break the 3D bulk transport problem into multiple 1D problems, each with a different transverse energy. The parameters used in modeling include the lattice constants of FM (2.89 Å) and MgO (4.05 Å) taken from crystallographic analysis and the effective mass of the electron in CoFeB ($0.8m_0$) and MgO (0.2 to $0.33m_0$) varied to fit experimental results considering impurity diffusion in the barrier and multi-domain FM system, along with the obtained barrier height of MgO (ϕ_B or $U_b = 0.9$ to 1.2 eV). The exchange splitting in CoFeB was chosen to be 2.15 eV, while the Fermi energy level of CoFeB was set to 2.25 eV, as adopted from Datta et al.³⁴

Figure 5c depicts the bias dependent conduction characteristics in the parallel state configuration. The differential tunneling conductance was calculated by $g(V) = dI/dV$ for the as-deposited and annealed samples. It was observed that the annealed MTJ provides an enhanced conductance of 4.5 mS as compared to the as-deposited sample (1.85 mS). The tunneling current and TMR characteristics for both experiment and simulation are observed to be following each other in the read bias range (-0.28 to 0.4 V) with positive slope conductance. However, in the antiparallel state, the conductance for annealed MTJ does not alter much with bias ($0.01 < V_{bias} < 0.4$ V), producing a gradual increase in TMR. This constant conductance for the annealed MTJ has been

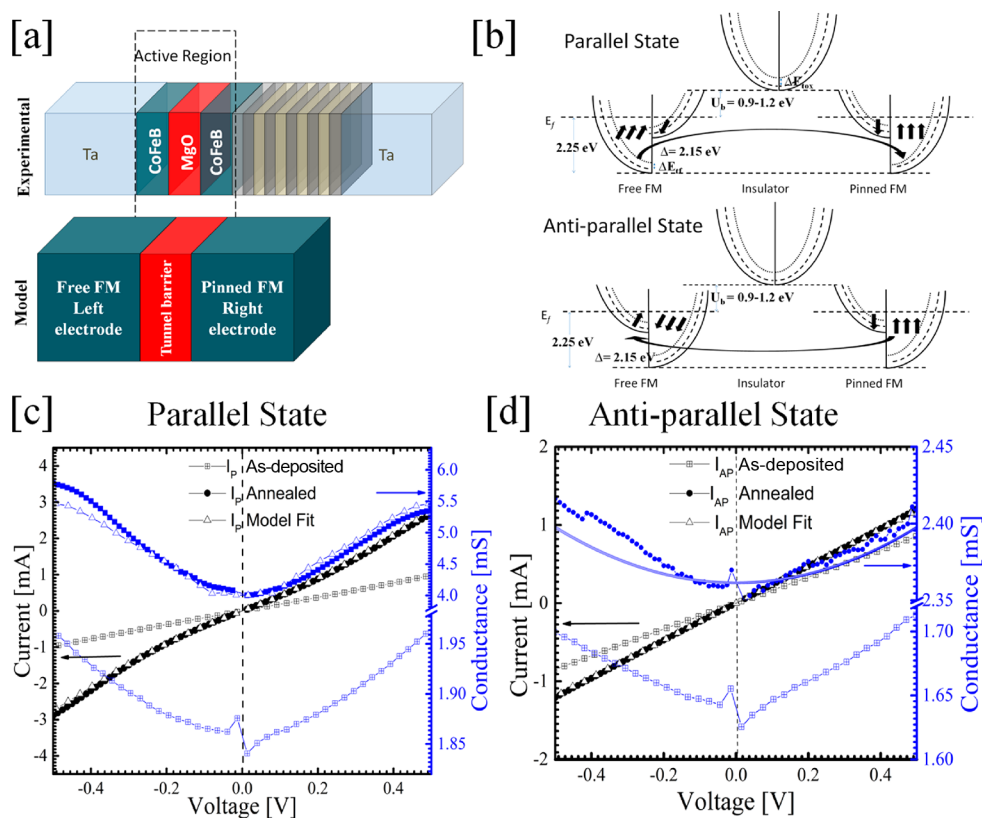


Figure 5. Tunneling analysis through the oxide barrier. (a) Schematic of a compact model for the active device regime; (b) energy band diagram for the analogous modeled MTJ. The left contact is a free FM layer, and an insulator (MgO) oxide introduces a tunneling barrier of height of 0.90–1.2 eV. The switching of free FM shows changes in conduction from parallel to antiparallel states. Experimental and numerical simulation of bias dependent characterization of p-MTJ for (c) parallel and (d) antiparallel configurations of MTJ; modeled electrical characteristics show a good match at low bias. Here, conductance $g(v)$ is shown in blue.

Table 1. Summary and Comparison of $[\text{Co}/\text{Pt}]_n$ or $[\text{Co}/\text{Pd}]_n$ -Based MTJs

MTJ stack structure (thickness in Å)	pinned layer	annealing (summary in K)	switching phenomena	TMR (%)	reference
Ta(50)/ $[\text{Co}(6)/\text{Pd}(18)]_x\text{Co}(07)/\text{MgO}(05)/\text{MgO}(21)\text{Co}(07)/[\text{Co}(7)/\text{Pd}(18)]_2$	-	423	FIS	11	Kugler et al. ⁴⁵
Ta(30)/Pt(100)/ $[\text{Co}(6)/\text{Pt}(18)]_4/\text{Co}(7)/\text{AlO}_x/[\text{Co}(7)/\text{Pt}(18)]_2/\text{Pt}(32)$	-	673	SMTE	15	Park et al. ⁴⁶
CoFeB(15)/MgO(10)/CoFeB(11)/Ta(04)/Co(05)/ $[\text{Co}/\text{Pt}](40)/\text{Ru}(8.5)/\text{Co}(05)/[\text{Co}/\text{Pt}](65)$	Ru, Hf, and Hf/Ru	673	SMTE	100	Chatterjee et al. ⁴⁷
CoFeB(10)/MgO(10)/CoFeB(15)/ $[\text{Co}/\text{Pt}](50)/\text{Ru}(8.5)/[\text{Co}/\text{Pt}](100)/\text{Ru}(50)$	$[\text{Co}/\text{Pt}]/\text{Ru}/[\text{Co}/\text{Pt}]/\text{Ru}$	598	STT-SOT	35	Kan et al. ⁴⁸
Ta(50)/ $[\text{Co}/\text{Pt}]_4/\text{Co}(80)/\text{Ta}(12)/\text{CoFeB}(20)/\text{MgO}(18)/\text{CoFeB}(20)/\text{Ta}(50)$	Co/ $[\text{Co}/\text{Pt}]_4$	650	STT	83	this work

^aThe abbreviations are FIS: field-induced switching; SMTE: spin-momentum transfer effect; and STT: spin-transfer torque effect.

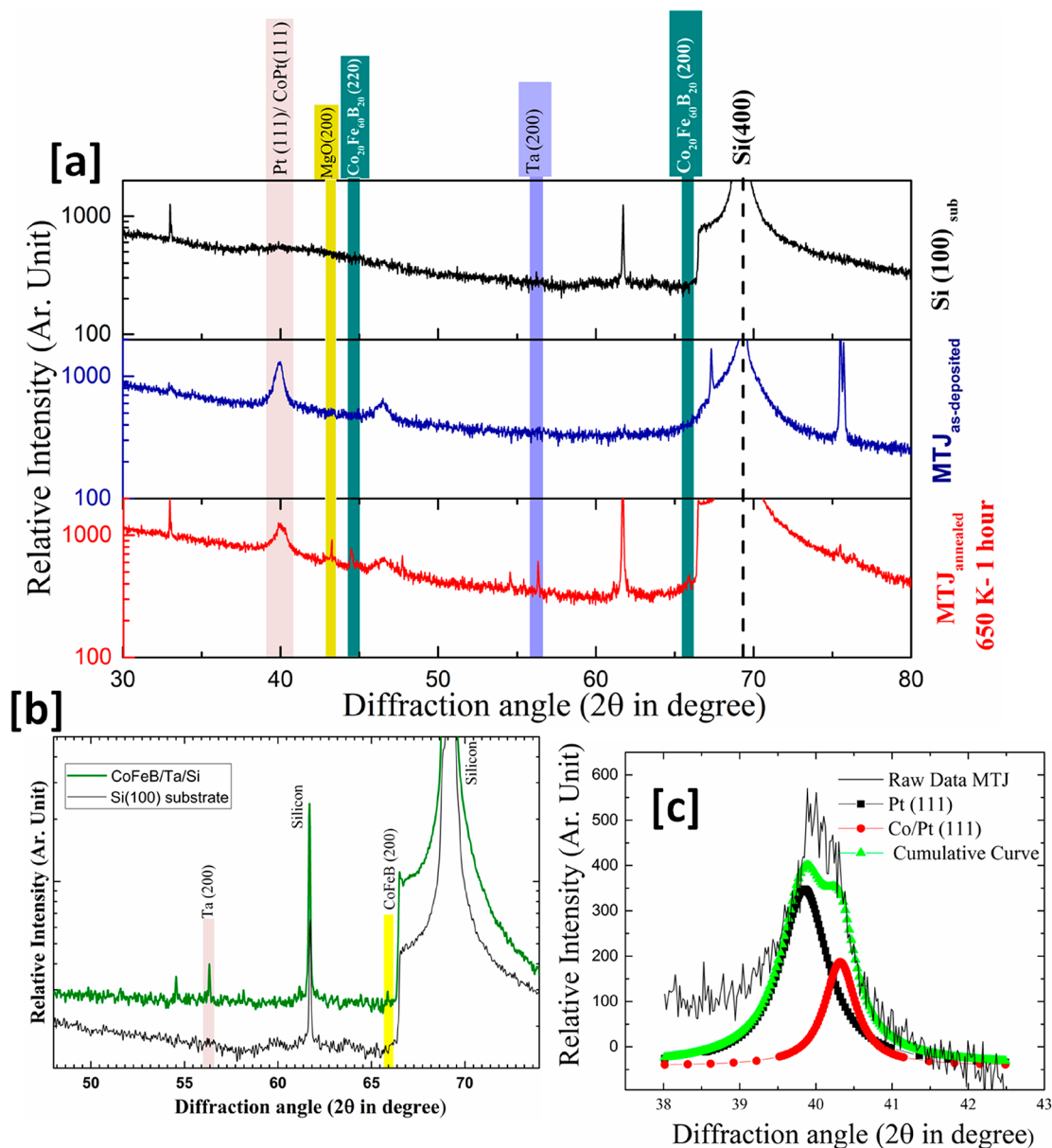


Figure 6. (a) X-ray diffraction (XRD) spectra of fabricated MTJ (as-deposited and annealed). Comparison of the bare substrate, as-deposited, and annealed samples showed crystallization after annealing. (b) XRD of free layer $\text{Co}_{20}\text{Fe}_{60}\text{B}_{20}(2)/\text{Ta}(5)/\text{Si}$ as a control sample. (c) Fitted curve with possible peaks for annealed MTJ; convoluted peaks showed the appearance of Pt (111) contact electrodes and a Co/Pt (111) SAF layer.

explained due to the multi-domain pinning in the antiparallel state after crystallization.⁴¹ Considering the large area free layer, the fitted model also showed constant conduction for the

bias region as shown in Figure 5d. The modeled results are in close agreement in the parallel state throughout the bias range; while in the antiparallel state, there is a good match in the low

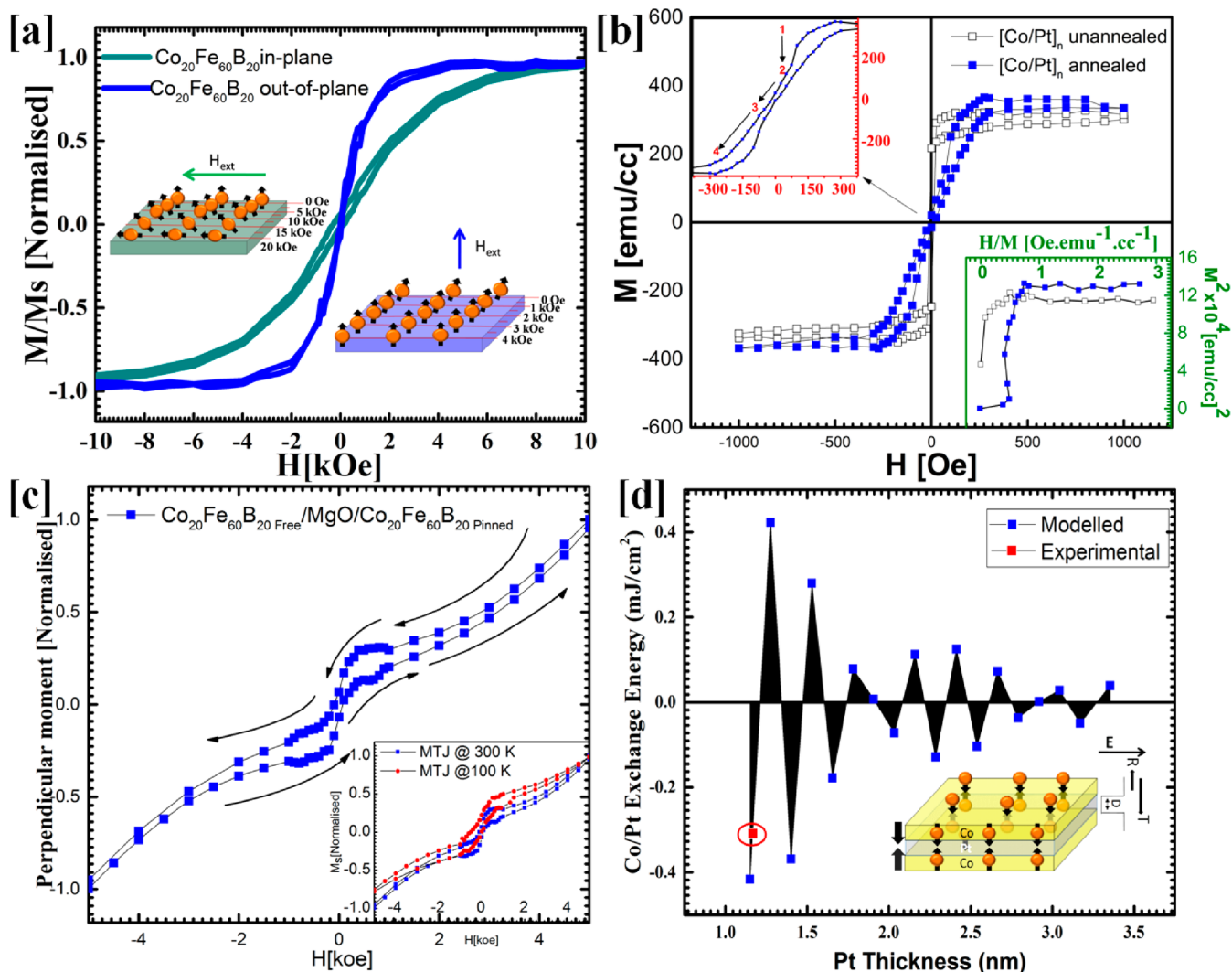


Figure 7. VSM hysteresis loops measured (a) in-plane and out-of-plane field hysteresis loops of the thin free layer with ~ 2 nm after annealing at 650 K (375 °C). The $M-H$ loop shows the out-of-plane easy axis getting saturated at 2.5 kOe (as shown in schematics) (b) for the Co/Pt multilayer. (c) Out-of-plane $M-H$ hysteresis loop for p-MTJ blanket with Pt/[Co/Pt]₄/Co/Ta/Co₂₀Fe₆₀B₂₀/MgO/Co₂₀Fe₆₀B₂₀/Ta/Pt/SiO₂/Si stacks. The low-temperature (100 K) $M-H$ depicts the dominant anti-ferromagnetic behavior of Co/Pt below TB (shown in inset). (d) Modeled [Co/Pt/Co] SAF showing oscillation in AFM-FM ordering with variation in spacer (Pt) thickness and an analogous schematic sketch of spin coupling (inset).

bias (± 0.4 V).⁴³ We make note that small modifications were done with the effective mass of MgO, which can be justified due to the small impurities in the ultrathin oxide tunneling layer, as it can alter the band structure of MgO, so the effective

$$\text{mass } m_0^* \propto \left(\frac{1}{h^2} \frac{d^2 E}{dk^2} \right)^{-1}.^{22,25,44}$$

The electrical performance of the investigated Ta/[Co/Pt]₄/Co/Ta/Co₂₀Fe₆₀B₂₀/MgO/Co₂₀Fe₆₀B₂₀/Ta p-MTJ structures showed promising STT-based device operation with enhanced TMR while reducing the stack size and materials used. Table 1 presents a summarized comparison of the present work with the previously reported [Co/Pt]_n-based MTJ structures.

3.2. Crystal Structure Analysis: Annealing Effect on p-MTJ Structures. XRD is used to confirm the crystal orientation of high-quality, nanoscale-thin Ta/[Co/Pt]₄/Co/Ta/CoFeB/MgO/CoFeB/Ta/Pt/Ti/SiO₂ p-MTJ multilayer structures. Figure 6a shows the XRD spectra of the as-deposited and annealed p-MTJ at 650 K (375 °C) for 1 h. For

the as-deposited films, the absence of specific desirable signature peaks in the MTJ blanket spectrum indicates the amorphous behavior.⁴⁹ On the other hand, the XRD spectra for the annealed MTJ blanket clearly reveal the crystallization of Co₂₀Fe₆₀B₂₀ and Ta buffer layer in the (200) crystal orientation on either side of the tunnel barrier layer. Figure 6b provides a clear understanding of the post annealing crystallization of the Co₂₀Fe₆₀B₂₀ FL with a Ta seed layer, i.e., only a two-layer structure as a control experiment versus the test MTJ stack structures. The orientation of (200) Co₂₀Fe₆₀B₂₀ crystal planes were observed under the influence of the Ta seed layer (200) crystal planes.^{50,51}

It is also be seen that Pt bottom and top electrodes' thin films exhibit the most stable fcc (111) orientation, along with other trivial (200) peaks. There is a significant peak shift in Pt (111) observed in the postannealed MTJ blanket. As Figure 6a consists of a bottom Pt layer (30 nm) and top [Co/Pt]₄ layers (9 nm), this shift in peak position can be attributed to the enhancement of the [Co/Pt]₄ (111) crystal orientation. Figure

6c represents the detailed peak position of the fcc Pt (111) and fcc Co/Pt (111) oriented multilayer system. The superimposed spectra of diffraction peaks of Co (111) and Pt (111) in fcc $[\text{Co/Pt}]_4$ expresses the crystalline nature of the multilayer system. The XRD spectra of the annealed Co/Pt multilayer stack does not present any peak trace at 20° , which suggests the absence of the L1_1 CoPt alloy.⁵² Post annealing, the $[\text{Co/Pt}]_4$ multilayers get anti-ferromagnetically coupled and act as an SAF as shown in Figure 7b. The contributions of the fcc Pt (111) bottom layer and fcc Co/Pt (111) SAF have been studied, and their separate contributions are confirmed in p-MTJ (as shown in Figure S7).⁵³

3.3. Magnetic Response Analysis: Origin of Free Layer, SAF, and Pinning the Reference Layer. To verify the existence of perpendicular magnetic anisotropy (PMA) with well-defined magnetization switching behavior in $\text{Co}_{20}\text{Fe}_{60}\text{B}_{20}$, the FL was probed under an external field. Figure 7a shows the dependence of magnetization (M_{sat}) of FL with the external field in-plane and out-of-plane of the film surface. The saturation in perpendicular magnetization around the ~ 3 kOe indicates an out-of-plane easy axis of the $\text{Co}_{20}\text{Fe}_{60}\text{B}_{20}$ FL. On the other hand, the measured in-plane M – H orientation of $\text{Co}_{20}\text{Fe}_{60}\text{B}_{20}$ showed unsaturated behavior indicating the hard axis. The out-of-plane anisotropy of the FL starts dominating with decreasing film thickness and results in an out-of-plane easy axis orientation.^{54,55} The schematic in Figure 7a illustrates the magnetization saturation under different values of the external magnetic field. The FM dipoles with the perpendicular easy axis require significantly less energy to align with the out-of-plane magnetic field as compared to the in-plane magnetic field.

The magnetic response for the Co/Pt multilayer stack was analyzed for confirmation of anti-ferromagnetic ordering. The response showed a hysteresis loop that indicates the combined response of the multilayer stack instead of a layer by layer switching response. Figure 7b shows the M – H response of the Co/Pt multilayer stack and the effect of annealing on the magnetic ordering. The as-deposited sample showed the absence of anti-ferromagnetic behavior while annealing up to 650 K (375°C) allowed crystallizing toward (111) orientation and effective exchange coupling between two consecutive Co layers. As shown in the loop ($1 \rightarrow 2 \rightarrow 3 \rightarrow 4$) (left inset), the hysteresis region ($1 \rightarrow 2$) is following a different slope than for the increasing magnetization path ($3 \rightarrow 4$). The non saturating portion of the curve ($3 \rightarrow 4$) in increasing field ($0 \rightarrow \pm 200$ Oe) indicates a reverse remnant magnetization that may be attributed to the existence of dissimilar bubble domains.¹⁹ These bubble domains eventually align at the high magnetic field. At decreasing applied field ($\pm 200 \rightarrow 0$ Oe), the hysteresis region shows sharp decay, which indicates the reversal of the same bubble domains that were aligned at high field. These domains are anti-ferromagnetically ordered up to 200 Oe. The Arrot plot (Figure 7b (right inset)) provides the evidence of non saturating AFM in an SAF layer for a low field.^{56–59} These $[\text{Co/Pt}]_4$ and SAF get coupled with $\text{Co}_{20}\text{Fe}_{60}\text{B}_{20}$, resulting in the pinning of the RL.

Figure 7c shows the hysteresis loops for the fabricated p-MTJ blanket. In contrast with FL magnetization (Figure 7a), the M – H loop of the fabricated p-MTJ structures depicts the FM–SAF ferromagnetic coupling justified by the increased coercivity of ~ 200 Oe (higher than FL ≈ 50 Oe).⁶⁰

The observed M – H curve describes the FL switching followed by RL switching in the high-field regime due to RL/

SAF coupling. The nonsaturating behavior of the M – H loop shows the anti-ferromagnetic coupling between Co/Pt/Co layers, which dominate at temperatures (figure shows 100 K) below the blocking temperature as shown in Figure 7c (inset).

The anti-ferromagnetic exchange coupling in crystalline $[\text{Co/Pt}]_4$ multilayers, a trilayer system, was modeled by using two-dimensional quantum well theory⁶¹ as shown in Figure 7d. The theoretical work function difference of 0.93 eV between Co (5.0 eV) and Pt (5.93 eV) results in a potential well between two ferromagnetic layers (Co/Pt/Co). It induces an oscillatory behavior in spin density with respect to the Pt thickness, resulting in a periodic oscillatory behavior of interlayer exchange energy (J) as shown in Figure 7d. It should be noted that J damps as $1/D^2$ where D is the thickness of the Pt layer. The simulated outcomes show anti-ferromagnetic behavior at 1.2 nm thick Pt layers, in agreement with the Pt (1.2 nm) thickness in the fabricated p-MTJ device structures. Thus, simulation and experimental results have investigated the use of single stack $[\text{Co/Pt}]_4$ for pinning RL.

4. CONCLUSION

In summary, we investigated the current-induced switching of a $\text{Co}_{20}\text{Fe}_{60}\text{B}_{20}/\text{MgO}/\text{Co}_{20}\text{Fe}_{60}\text{B}_{20}$ -based p-MTJ with a $[\text{Co/Pt}]_4$ stack as the SAF. Electrical and spectroscopic evidence reveal the pinning of the $\text{Co}_{20}\text{Fe}_{60}\text{B}_{20}$ layer by SAF through a Ta spacer layer, which enhances the switching resistance after annealing at 650 K (375°C). A 600% increase in TMR was observed after annealing in an external magnetic field (14% for as-deposited and 83% for annealed both for zero bias). The TMR also shows the novel behavior of a gradual increase with bias at room temperature, which may be attributed to the multi-domain switching with increase in current. The analogous SAF based MTJ devices were modeled using NEGF to validate the experimental results. The existence of a stable TMR and the low switching current density of the fabricated p-MTJ structures provides higher reliability and low-power operation. This makes it attractive for next-generation MTJ applications, especially for embedded memory, system-on-chip, IoT, and neuromorphic computing applications.

■ ASSOCIATED CONTENT

📄 Supporting Information

The Supporting Information is available free of charge on the ACS Publications website at DOI: 10.1021/acsaem.9b00469.

Morphological analysis of the fabricated devices along with the surface roughness of the free layer (Figure S1); boron (B) distribution inside $\text{Co}_{20}\text{Fe}_{60}\text{B}_{20}$ FL and MTJ blanket confirmed using elemental analysis (Figure S2); calculation of barrier height characteristics of the tunnel barrier devices (Figures S3 and S4); proposed switching mechanism based on device experimental data (Figures S5 and S6); crystallographic evidence of $[\text{Co/Pt}]_n$ SAF (PDF)

■ AUTHOR INFORMATION

Corresponding Author

*E-mail: satinder@iitmandi.ac.in.

ORCID

Satinder K. Sharma: 0000-0001-9313-5550

Notes

The authors declare no competing financial interest.

ACKNOWLEDGMENTS

This work was supported under the financial support of IIT Mandi seed grant IITM/SG/SS/62. The authors thank the C4DFED and AMRC centers at IIT Mandi for providing device fabrication, characterization, and materials characterization facilities; the Nanoscience Centre, IIT Kanpur for assistance in X-ray diffraction analysis; Mr. Ratul Paul from Thermo-Fisher for depth profile analysis; and Dr. Mahesh Soni and Ms. Shivangi Shringi from SCEE, IIT Mandi for valuable discussions. MGM is supported under the “Visvesvaraya PhD Scheme” by MEITY, India.

REFERENCES

- (1) Chen, A. A Review of Emerging Non-Volatile Memory (NVM) Technologies and Applications. *Solid-State Electron.* **2016**, *125*, 25–38.
- (2) Chappert, C.; Fert, A.; Van Dau, F. N. The Emergence of Spin Electronics in Data Storage. *Nat. Mater.* **2007**, *6* (11), 813–823.
- (3) Kim, N. S.; Austin, T.; Blaauw, D.; Mudge, T.; Flautner, K.; Hu, J. S.; Irwin, M. J.; Kandemir, M.; Narayanan, V. Leakage Current: Moore’s Law Meets Static Power. *IEEE Comput.* **2003**, *36* (12), 68–75.
- (4) Kang, W.; Ran, Y.; Zhang, Y.; Lv, W.; Zhao, W. Modeling and Exploration of the Voltage-Controlled Magnetic Anisotropy Effect for the Next-Generation Low-Power and High-Speed MRAM Applications. *IEEE Trans. Nanotechnol.* **2017**, *16* (3), 387–395.
- (5) Bader, S. D.; Parkin, S. S. P. Spintronics. *Annu. Rev. Condens. Matter Phys.* **2010**, *1* (1), 71–88.
- (6) Tehrani, S.; Slaughter, J. M.; Chen, E.; Durlam, M.; Shi, J.; DeHerren, M. Progress and Outlook for MRAM Technology. *IEEE Trans. Magn.* **1999**, *35* (5), 2814–2819.
- (7) Gallagher, W. J.; Parkin, S. S. P.; Lu, Y.; Bian, X. P.; Marley, A.; Roche, K. P.; Altman, R. A.; Rishton, S. A.; Jahnke, C.; Shaw, T. M.; et al. Microstructured Magnetic Tunnel Junctions. *J. Appl. Phys.* **1997**, *81* (8), 3741–3746.
- (8) Sankey, J. C.; Cui, Y. T.; Sun, J. Z.; Slonczewski, J. C.; Buhrman, R. A.; Ralph, D. C. Measurement of the Spin-Transfer-Torque Vector in Magnetic Tunnel Junctions. *Nat. Phys.* **2008**, *4* (1), 67–71.
- (9) Kan, J. J.; Park, C.; Ching, C.; Ahn, J.; Xie, Y.; Pakala, M.; Kang, S. H. A Study on Practically Unlimited Endurance of STT-MRAM. *IEEE Trans. Electron Devices* **2017**, *64* (9), 3639–3646.
- (10) Iyengar, A.; Ghosh, S.; Srinivasan, S. Retention Testing Methodology for STTRAM. *IEEE Des. Test* **2016**, *33* (5), 7–15.
- (11) Chun, K. C.; Zhao, H.; Harms, J. D.; Kim, T. H.; Wang, J. P.; Kim, C. H. A Scaling Roadmap and Performance Evaluation of In-Plane and Perpendicular MTJ Based STT-MRAMs for High-Density Cache Memory. *IEEE J. Solid-State Circuits* **2013**, *48* (2), 598–610.
- (12) Driskill-Smith, A.; Apalkov, D.; Nikitin, V.; Tang, X.; Watts, S.; Lottis, D.; Moon, K.; Khvalkovskiy, A.; Kawakami, R.; Luo, X.; Ong, a.; Krombi, M.; et al. Latest Advances and Roadmap for In-Plane and Perpendicular STT-RAM. *2011 3rd IEEE International Memory Workshop (IMW)* **2011**, 1–3.
- (13) Salahuddin, S. *Novel Electronic and Spintronic Devices for Low Power Logic Computation*, Ph.D. Thesis, Purdue University, 2007.
- (14) Huai, Y.; Gan, H.; Wang, Z.; Xu, P.; Hao, X.; Yen, B. K.; Malmhall, R.; Pakala, N.; Wang, C.; Zhang, J.; Zhou, Y.; Jung, D.; Satoh, K.; Wang, R.; Xue, L.; Pakala, M. High Performance Perpendicular Magnetic Tunnel Junction with Co/Ir Interfacial Anisotropy for Embedded and Standalone STT-MRAM Applications. *Appl. Phys. Lett.* **2018**, *112* (9), 092402.
- (15) Hirohata, A.; Sukegawa, H.; Yanagihara, H.; Zutic, I.; Seki, T.; Mizukami, S.; Swaminathan, R. Roadmap for Emerging Materials for Spintronic Device Applications. *IEEE Trans. Magn.* **2015**, *51* (10), 1.
- (16) Chen, J. Y.; Lau, Y. C.; Coey, J. M. D.; Li, M.; Wang, J. P. High Performance MgO-Barrier Magnetic Tunnel Junctions for Flexible and Wearable Spintronic Applications. *Sci. Rep.* **2017**, *7*, 42001.
- (17) Bandiera, S.; Sousa, R. C.; Dahmane, Y.; Ducruet, C.; Portemont, C.; Baltz, V.; Auffret, S.; Prejbeanu, I. L.; Dieny, B. Comparison of Synthetic Antiferromagnets and Hard Ferromagnets as Reference Layer in Magnetic Tunnel Junctions with Perpendicular Magnetic Anisotropy. *IEEE Magn. Lett.* **2010**, *1*, 3000204.
- (18) Lee, Y. M.; Hayakawa, J.; Ikeda, S.; Matsukura, F.; Ohno, H. Giant Tunnel Magnetoresistance and High Annealing Stability in CoFeB/MgO/CoFeB Magnetic Tunnel Junctions with Synthetic Pinned Layer. *Appl. Phys. Lett.* **2006**, *89* (4), 042506.
- (19) Hellwig, O.; Kirk, T. L.; Kortright, J. B.; Berger, A.; Fullerton, E. E. A New Phase Diagram for Layered Antiferromagnetic Films. *Nat. Mater.* **2003**, *2* (2), 112–116.
- (20) Babcock, K. L.; Westervelt, R. M. Avalanches and Self-Organization in Cellular Magnetic-Domain Patterns. *Phys. Rev. Lett.* **1990**, *64* (18), 2168–2171.
- (21) Chamberod, A.; Marty, A.; Samson, Y.; Gilles, B.; Gehanno, V. Magnetic Susceptibility and Magnetic Domain Configuration as a Function of the Layer Thickness in Epitaxial FePd(0 0 1) Thin Films Ordered in the L1₀ Structure. *J. Magn. Magn. Mater.* **1997**, *172* (1–2), 26–40.
- (22) Lee, S. E.; Baek, J. U.; Park, J. G. Highly Enhanced TMR Ratio and Δ for Double MgO-Based p-MTJ Spin-Valves with Top Co₂Fe₆B₂ Free Layer by Nanoscale-Thick Iron Diffusion-Barrier. *Sci. Rep.* **2017**, *7*, 11907.
- (23) IEEE. *International Roadmap For Devices And Systems 2017 Edition*, 2017.
- (24) Sato, H.; Ikeda, S.; Fukami, S.; Honjo, H.; Ishikawa, S.; Yamanouchi, M.; Mizunuma, K.; Matsukura, F.; Ohno, H. Co/Pt Multilayer Based Reference Layers in Magnetic Tunnel Junctions for Nonvolatile Spintronics VLSIs. *Jpn. J. Appl. Phys.* **2014**, *53*, 04EM02.
- (25) Datta, D.; Behin-Aein, B.; Datta, S.; Salahuddin, S. Voltage Asymmetry of Spin-Transfer Torques. *IEEE Trans. Nanotechnol.* **2012**, *11* (2), 261–272.
- (26) Wang, C.; Cui, Y.-T.; Sun, J. Z.; Katine, J. A.; Buhrman, R. A.; Ralph, D. C. Bias and Angular Dependence of Spin-Transfer Torque in Magnetic Tunnel Junctions. *Phys. Rev. B: Condens. Matter Mater. Phys.* **2009**, *79* (22), 224416.
- (27) Ying, J. F.; Lim, S. T.; Tran, M.; Ji, R. Effects of Post-Growth Annealing in a CoFeB/MgO/CoFeB Trilayer Structure. *J. Phys. D: Appl. Phys.* **2015**, *48* (45), 455001.
- (28) Hindmarch, A. T.; Harnchana, V.; Walton, A. S.; Brown, A. P.; Brydson, R. M. D.; Marrows, C. H. Zirconium as a Boron Sink in Crystalline CoFeB/MgO/CoFeB Magnetic Tunnel Junctions. *Appl. Phys. Express* **2011**, *4* (1), 013002.
- (29) Gehring, A.; Selberherr, S. Tunneling Models for Semiconductor Device Simulation. *Handbook of Theoretical and Computational Nanotechnology*; American Scientific Publishers, 2006; Vol. 10, pp 469–543.
- (30) Wang, W.; Lee, T.; Reed, M. A. Intrinsic Electronic Conduction Mechanisms in Self-Assembled Monolayers. *Lect. Notes Phys.* **2006**, *680*, 275–300.
- (31) Fetzter, R.; Stadtmüller, B.; Ohdaira, Y.; Naganuma, H.; Oogane, M.; Ando, Y.; Taira, T.; Uemura, T.; Yamamoto, M.; Aeschlimann, M.; Cinchetti, M. Probing the Electronic and Spintronic Properties of Buried Interfaces by Extremely Low Energy Photoemission Spectroscopy. *Sci. Rep.* **2015**, *5*, 1–6.
- (32) Useinov, A.; Ye, L. X.; Useinov, N.; Wu, T. H.; Lai, C. H. Anomalous Tunnel Magnetoresistance and Spin Transfer Torque in Magnetic Tunnel Junctions with Embedded Nanoparticles. *Sci. Rep.* **2016**, *5* (July), 1–9.
- (33) Kaiju, H.; Takei, M.; Misawa, T.; Nagahama, T.; Nishii, J.; Xiao, G. Large Magnetocapacitance Effect in Magnetic Tunnel Junctions Based on Debye-Fröhlich Model. *Appl. Phys. Lett.* **2015**, *107* (13), 132405.
- (34) Sahadevan, A. M.; Gopinadhan, K.; Bhatia, C. S.; Yang, H. Parallel-Leaky Capacitance Equivalent Circuit Model for MgO Magnetic Tunnel Junctions. *Appl. Phys. Lett.* **2012**, *101* (16), 162404.
- (35) Wang, X.; Iniewski, K. In *Metallic Spintronic Devices*; Wang, X., Ed.; CRC Press, 2014.

- (36) Li, S.; Jones, A. K.; Zhang, Y.; Wang, X.; Li, Y.; Chen, Y. Spin Transfer Torque-RAM Devices as a Future Non-Volatile Memory Solution. *2012 Des. Autom. Test Eur. Conf. Exhib.* **2015**, 1–6.
- (37) Park, C.; Zhu, J.-G.; Moneck, M. T.; Peng, Y.; Laughlin, D. E. Annealing Effects on Structural and Transport Properties of Rf-Sputtered Magnetic Tunnel Junctions. *J. Appl. Phys.* **2006**, *99*, 08A901.
- (38) Tamanoi, K.; Sato, M.; Oogane, M.; Ando, Y.; Tanaka, T.; Uehara, Y.; Uzumaki, T. Electrical Conductance Properties for Magnetic Tunnel Junctions with MgO Barriers. *J. Magn. Magn. Mater.* **2008**, *320* (22), 2959–2962.
- (39) Chen, E.; Schwarz, B.; Choi, C. J.; Kula, W.; Wolfman, J.; Ounadjela, K.; Geha, S. Magnetic Tunnel Junction Pattern Technique. *J. Appl. Phys.* **2003**, *93* (10), 8379–8381.
- (40) Sharma, A.; Hoffmann, M. A.; Matthes, P.; Kohler, N.; Busse, S.; Muller, M.; Exner, H.; Schulz, S. E.; Zahn, D. R. T.; Salvan, G. Magnetic Tunnel Junctions: Laser Annealing versus Oven Annealing. *IEEE Trans. Magn.* **2019**, *55* (1), 1–4.
- (41) Chanthbouala, A.; Matsumoto, R.; Grollier, J.; Cros, V.; Anane, A.; Fert, A.; Khvalkovskiy, A. V.; Zvezdin, K. A.; Nishimura, K.; Nagamine, Y.; et al. Vertical-Current-Induced Domain-Wall Motion in MgO-Based Magnetic Tunnel Junctions with Low Current Densities. *Nat. Phys.* **2011**, *7* (4), 626.
- (42) Enobio, E. C. L.; Bersweiler, M.; Sato, H.; Fukami, S.; Ohno, H. Evaluation of Energy Barrier of CoFeB/MgO Magnetic Tunnel Junctions with Perpendicular Easy Axis Using Retention Time Measurement. *Jpn. J. Appl. Phys.* **2018**, *57* (4S), 04FN08.
- (43) Nedelkoski, Z.; Kepaptsoglou, D.; Lari, L.; Wen, T.; Booth, R. A.; Oberdick, S. D.; Galindo, P. L.; Ramasse, Q. M.; Evans, R. F. L.; Majetich, S.; Lazarov, V. K. Origin of Reduced Magnetization and Domain Formation in Small Magnetite Nanoparticles. *Sci. Rep.* **2017**, *7*, 1–8.
- (44) Kalitsov, A.; Andrieu, S.; Tiusan, C.; Velev, J. P.; Zermatten, P.-J.; Bonell, F.; Gaudin, G.; Chshiev, M. Bias Dependence of Tunneling Magnetoresistance in Magnetic Tunnel Junctions with Asymmetric Barriers. *J. Phys.: Condens. Matter* **2013**, *25* (49), 496005.
- (45) Schmalhorst, J.; Reiss, G.; Drewello, V.; Thomas, A.; Kugler, Z.; Schäfers, M. Temperature and Bias Voltage Dependence of Co/Pd Multilayer-Based Magnetic Tunnel Junctions with Perpendicular Magnetic Anisotropy. *J. Magn. Magn. Mater.* **2011**, *323* (2), 198–201.
- (46) Park, J.-H.; Zhu, J.-G.; Park, C.; Jeong, T.; Moneck, M. T.; Nufer, N. T. Co/Pt Multilayer Based Magnetic Tunnel Junctions Using Perpendicular Magnetic Anisotropy. *J. Appl. Phys.* **2008**, *103* (7), 07A917.
- (47) Chatterjee, J.; Tahmasebi, T.; Swerts, J.; Kar, G. S.; De Boeck, J. Impact of Seed Layer on Post-Annealing Behavior of Transport and Magnetic Properties of Co/Pt Multilayer-Based Bottom-Pinned Perpendicular Magnetic Tunnel Junctions. *Appl. Phys. Express* **2015**, *8* (6), 063002.
- (48) Wang, M.; Cai, W.; Zhu, D.; Wang, Z.; Kan, J.; Zhao, Z.; Cao, K.; Wang, Z.; Zhang, Y.; Zhang, T.; et al. Field-Free Switching of a Perpendicular Magnetic Tunnel Junction through the Interplay of Spin-Orbit and Spin-Transfer Torques. *Nat. Electron.* **2018**, *1* (11), 582–588.
- (49) Jian, Z.; Hejing, W. The Physical Meanings of 5 Basic Parameters for an X-Ray Diffraction Peak and Their Application. *Chin. J. Geochem.* **2003**, *22* (1), 38–44.
- (50) Ikeda, S.; Miura, K.; Yamamoto, H.; Mizunuma, K.; Gan, H. D.; Endo, M.; Kanai, S.; Hayakawa, J.; Matsukura, F.; Ohno, H. A Perpendicular-Anisotropy CoFeB-MgO Magnetic Tunnel Junction. *Nat. Mater.* **2010**, *9* (9), 721–724.
- (51) Ikeda, S.; Hayakawa, J.; Ashizawa, Y.; Lee, Y. M.; Miura, K.; Hasegawa, H.; Tsunoda, M.; Matsukura, F.; Ohno, H. Tunnel Magnetoresistance of 604% at 300 K by Suppression of Ta Diffusion in CoFeBMgOCoFeB Pseudo-Spin-Valves Annealed at High Temperature. *Appl. Phys. Lett.* **2008**, *93* (8), 082508.
- (52) Honda, N.; Hinata, S.; Saito, S. Layer Stacked Co/Pt Films with High Perpendicular Anisotropy Sputter Deposited at Room Temperature. *AIP Adv.* **2017**, *7* (5), 056518.
- (53) Canedy, C.; Li, X.; Xiao, G. Large Magnetic Moment Enhancement and Extraordinary Hall Effect in Co/Pt Superlattices. *Phys. Rev. B: Condens. Matter Mater. Phys.* **2000**, *62* (1), 508–519.
- (54) Nakano, T.; Oogane, M.; Furuichi, T.; Ao, K.; Naganuma, H.; Ando, Y. Magnetic Tunnel Junctions with [Co/Pd]-Based Reference Layer and CoFeB Sensing Layer for Magnetic Sensor. *IEEE Trans. Magn.* **2016**, *52* (7), 4001304.
- (55) Hu, G.; Topuria, T.; Rice, P. M.; Jordan-Sweet, J.; Worledge, D. C. Optimization of Tunneling Magnetoresistance in Perpendicular Magnetic Tunnel Junctions With CoPd Reference Layers. *IEEE Magn. Lett.* **2013**, *4*, 3000104–3000104.
- (56) Xu, Z.; Gong, W.; Lin, A.; Zhang, Y.; Wang, L.; Zhang, Y. Magnetocaloric Properties in the PrFe₂Ge₂ Antiferromagnet. *2015 International Conference on Structural, Mechanical and Material Engineering* **2015**, 120–123.
- (57) Obinata, A.; Hibino, Y.; Hayakawa, D.; Koyama, T.; Miwa, K.; Ono, S.; Chiba, D. Electric-Field Control of Magnetic Moment in Pd. *Sci. Rep.* **2015**, *5*, 1–10.
- (58) Yeung, I.; Roshko, R. M.; Williams, G. Arrott-Plot Criterion for Ferromagnetism in Disordered Systems. *Phys. Rev. B: Condens. Matter Mater. Phys.* **1986**, *34* (5), 3456–3457.
- (59) Arrott, A. Criterion for Ferromagnetism from Observations of Magnetic Isotherms. *Phys. Rev.* **1957**, *108* (6), 1394–1396.
- (60) Nogués, J. N.; Schuller, I. K. Exchange Bias. *J. Magn. Magn. Mater.* **1999**, *192*, 203–232.
- (61) Duine, R. A.; Lee, K. J.; Parkin, S. S. P.; Stiles, M. D. Synthetic Antiferromagnetic Spintronics. *Nat. Phys.* **2018**, *14* (3), 217–219.